Eu³⁺-Based Bridged Silsesquioxanes for Transparent Luminescent Solar Concentrators

Vânia. T. Freitas,[†,‡] Lianshe Fu,[†] Ana M. Cojocariu,[§,⊥] Xavier Cattoën,[§,#] John R. Bartlett,[⊥] Rozenn Le Parc,[‡] Jean-Louis Bantignies,*[,‡] Michel Wong Chi Man,[§] Paulo S. André,[∥] Rute A. S. Ferreira,[†] and Luís D. Carlos*[,†]

[†]Physics Department and CICECO Aveiro Institute of Materials, University of Aveiro, 3810-193 Aveiro, Portugal

[‡]Laboratoire Charles Coulomb (L2C), UMR 5521 CNRS-Université de Montpellier, 34095 Montpellier, France

[§]Institut Charles Gerhardt Montpellier, UMR 5253 CNRS-UM2-ENSCM-UM1, 34296 Montpellier, France

[⊥]Faculty of Science, Health, Education and Engineering, University of the Sunshine Coast, Maroochydore DC, QLD 4558 Australia

[#]Institut NEEL, CNRS, Université Grenoble-Alpes, 38042 Grenoble, France

[∥]Department of Electric and Computer Engineering and Instituto de Telecomunicações, Instituto Superior Técnico, Universidade de Lisboa, Lisboa, Portugal

ⓢ Supporting Information

ABSTRACT: The sol−gel preparation of a bridged silsesquioxane containing europium(III) salts and 2-thenoyltrifluoroacetone has been achieved from a new ethane tetracarboxamide-based organosilane. Free-standing films with thicknesses up to 440 μm and maximum absolute quantum yield (q) of 0.34 ± 0.03 (excitation at 320 nm) were prepared by the drop cast method, while thin films (∼200−400 nm) spin-coated on glass substrates led to highly luminescent coatings with q = 0.60 ± 0.02 (excitation at 345 nm). The thin films were tested as planar luminescent solar concentrators and the optimized device displays an optical conversion efficiency of 12.3% in the absorbing spectral region of the active layer (300−380 nm).
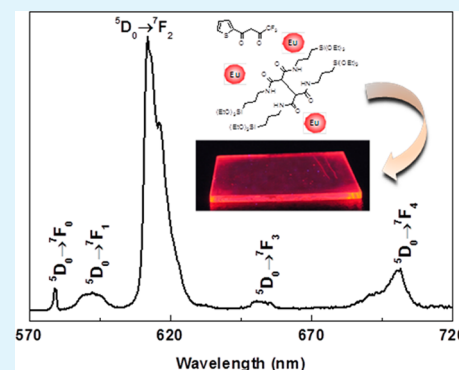
KEYWORDS: organic−inorganic hybrids, lanthanide complex, sol−gel, thin films, luminescent solar concentrator

■ INTRODUCTION

The peculiar emission features typical of lanthanides (Ln³⁺) ions, such as photostability, long lifetimes (>10⁻⁴ s), large Stokes/anti-Stokes shifts (>200 nm), narrow bandwidth emissions (full width at half-maximum, fwhm∼ 1 nm) lying from the UV to the near-infrared (NIR) spectral regions, high luminescence quantum yields (up to 0.9), and ligand-dependent sensitization, arise from the particular 4f electronic energy level configuration.[1−5] All of these features offer excellent prospects for designing new Ln³⁺-based luminescent materials with a wide range of applications as phosphors, in lighting and displays, in integrated optics and optical tele-communications, in solar cells, in sensors, and in biomedi-cine.[6−9] Furthermore, Ln³⁺ ions can be complexed by a wide variety of organic molecules, which harvest light and transfer energy efficiently onto the metal ions. The formation of complexes between Ln³⁺ ions and certain organic ligands has an extra beneficial effect, protecting metal ions from vibrational coupling and increasing the light absorption cross-section by ligand sensitization.[10] However, these Ln³⁺ complexes show a rather low thermal and photochemical stability, that together

with the poor mechanical properties and photodegradation upon UV exposure are important disadvantages concerning its technological applicability.[11,12]

One solution to improve the mechanical and optical properties of Ln³⁺-based complexes is to introduce them in a stable rigid matrix, for example, silica-based hybrid material. In this context, Ln³⁺-containing organic−inorganic hybrids are good candidates, combining the physical properties and functionalities of the inorganic network and/or the organic fragments with the Ln³⁺ luminescence.[1,13−18] Importantly, hybrid materials can easily be processed as transparent thin films with applicability in disparate domains, such as agriculture and horticulture,[15] lighting,[19] integrated optics, and optical telecommunications,[13,17] active coatings for improving the conversion efficiency of Si-based solar cells,[16] nanomedicine,[20] and for luminescent solar concentrators (LSCs).[21−25]

Ln^{3+}-containing bridged silsesquioxanes (BS)[26,27] obtained by hydrolysis−condensation of organo-bridged polytrialkoxysilanes (RO)$_3$Si−X−Si(OR)$_3$ (X = organic function, R = Et, Me) are able to incorporate a high loading of Ln^{3+} complexes (up to 11.2 wt %)[28] covalently bonded to the siloxane network being easily processed as thin films with excellent homogeneity and transparency.[28−35] These films are luminescent active coatings, whose applicability as LSCs was recently highlighted.[28,35] The concept of LSCs reappeared as a promising way to improve solar cells efficiency,[36] despite the first reports date from 1976.[37] LSCs are composed of films bearing optically active centers that collect the incident sunlight and reemit it partially at a specific wavelength. Part of this emitted light is trapped inside the layer and concentrated at the edge of the film, where it can be collected by a photovoltaic (PV) cell. The main requirements for efficient LSCs are (i) broad spectral absorption; (ii) high absorption efficiency; (iii) large Stokes shifts; (iv) high luminescence efficiency; and (v) emission energy resonant with the PV cell responsivity.[25] Promising results have been obtained for dye-based LSCs with an optical conversion efficiency (η_{opt}) of 18.8%.[38] The intrinsic small Stokes-shift of the dye molecules, however, induced high self-absorptions, which is a significant drawback. The use of large Stokes shift optically active centers, such as Ln^{3+} ions, is one way to cope with the large self-absorption losses observed in dye[38−42] and quantum dots (QDs)[42−44]-based LSCs.

Despite this potential, few works were published on Ln^{3+}-based LSCs providing quantitative evidence of the improvement of PV cells performance, e.g., Eu^{3+}-based LSCs pointing out an increase of 15%[21] and 12.5%[45] on the PV cell photocurrent and an enhancement of the power conversion efficiency of 0.28%,[24] 0.007%,[25] and 0.0441%.[46] Optical conversion efficiency values of Ln^{3+}-based LSCs were calculated for selected excitation wavelengths, namely 8.8%, for Tb^{3+}-based poly(vinyl alcohol) incorporating salicylic acid,[47] 9%, for Eu(tta)$_3$.ephen (ephen = 5,6-epoxy-5,6-dihydro[1,10] phenanthroline) embedded into a triureasil hybrid,[48] and 4.3% and 1.7%, for Eu^{3+}-[28] and Tb^{3+}-doped[35] BS, respectively. More recently, flexible waveguiding cylindrical LSCs based on plastic optical fibers coated with Eu^{3+}-doped organic−inorganic hybrids were demonstrated with optical conversion efficiency and power conversion efficiency values of 20.7 ± 1.3% and 2.5 ± 0.2%, respectively.[49]

In view of generalizing the use of Ln^{3+}−containing hybrid materials as LSCs, we developed here Eu^{3+}-bearing ethane tetracarboxamide-BS hybrids. Monoliths and thin films with controlled thickness were prepared by drop cast and spin-coating, respectively, and their structural and photophysical properties were characterized. Thin films with lower amount of optically Eu^{3+} centers (3% w/w) and combining tuned refractive index and high emission quantum yield (up to 0.60), were used to fabricate planar LSCs. The devices' performance was characterized and compared with that of transparent LSCs, demonstrating the potential of organic−inorganic hybrids to enhance PV conversion efficiency.

■ EXPERIMENTAL SECTION

The reagents (3-aminopropyl)triethoxysilane (APTES), tetraethyl ethanetetracarboxylate, ethanol (EtOH), 1-propanol (1-PrOH), dimethylformamide (DMF), methanol (MeOH), ammonium fluoride (NH$_4$F), europium chloride hexahydrate (EuCl$_3$·6H$_2$O), and 2-thenoyltrifluoroacetone (tta−H) are from Sigma-Aldrich company

and used as received without further purifications. EtOH was dried by distillation over Mg/I$_2$.

Synthesis of the Ethane Tetracarboxamide-Based Precursor. A mixture of APTES (10 mL, 43.0 mmol) and tetraethylethanetetracarboxylate (3.0 g, 9.4 mmol) placed under Ar in a sealed flask was heated at 100 °C for 18 h under vigorous stirring (Scheme 1). Upon

Scheme 1. Representation of the Synthesis Route of P4-m, M4-m-2, M4-m-3 and F6; Photographs Acquired under Daylight Illumination and UV Exposure (Spectroline ENF-280C/FE)
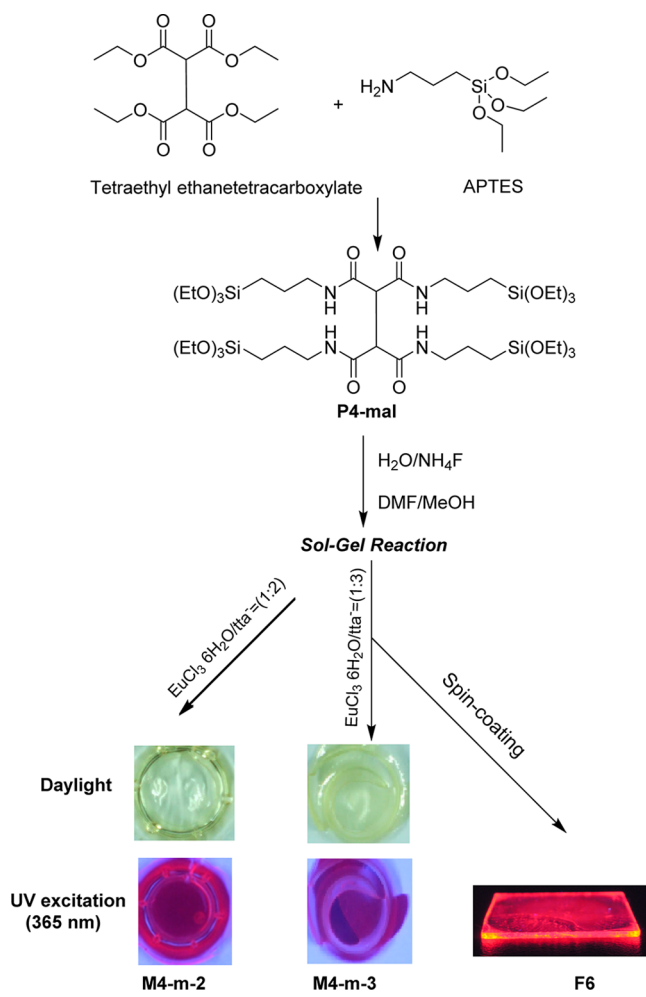
cooling, a solid was formed that was filtered and washed with anhydrous ethanol (3 × 10 mL) and then dried under vacuum. The precursor P4-m was obtained as a white powder (9.1 g, 94% yield). ^{1}H NMR (CDCl$_3$, 400 MHz): δ (ppm): 0.58 (m, 8 H), 1.19 (t, J = 7.0 Hz, 36 H), 1.57 (m, 8 H), 3.16 (m, 8 H), 3.78 (q, J = 7.0 Hz, 24 H), 4.05 (s, 2H), 7.41 (br, 4H). ^{13}C NMR (CDCl$_3$, 100 MHz): δ (ppm): 7.7, 18.3, 22.6, 42.5, 53.7, 58.3, 168.1.

Synthesis of the Eu^{3+}-Ethane Tetracarboxamide-Based Organic−Inorganic Hybrids. In the first stage, a solution of EuCl$_3$·6H$_2$O (35.5 mg, 0.097 mmol) in a mixture of DMF (0.74 mL) and MeOH (2.2 mL) (ratio of DMF/MeOH = 1/3 v/v, 1.0:5.7 molar ratio) was added to P4-m (300 mg, 0.294 mmol) and the mixture was heated at 60 °C until a clear solution was obtained. Then distilled H$_2$O (129.4 μL, 7.16 mmol) was added and the solution was stirred for 20 min at 60 °C. Finally, 0.1 M NH$_4$F (29.4 μL, 0.00294 mmol) was added. The final molar ratio was P4-m:H$_2$O:NH$_4$F:EuCl$_3$·6H$_2$O = 1:30:0.01:0.33. A white powder was obtained, being identified as M4-m-1. Aiming at enhancing the light harvesting ability of the Eu^{3+}−doped hybrids the chromophore tta−H was also incorporated

(Scheme 1). $EuCl_3 \cdot 6H_2O$ (35.5 mg) and tta-H (43.1 mg for M4-m-2 or 64.7 mg for M4-m-3) were added to P4-m, with a ratio P4-m:H_2O:NH_4F:$EuCl_3 \cdot 6H_2O$:tta-H = 1:30:0.01:0.33:0.66 for (M4-m-2), and P4-m:H_2O:NH_4F:$EuCl_3 \cdot 6H_2O$:tta-H = 1:30:0.01:0.33:0.99 for (M4-m-3), following a similar procedure as used to prepare M4-m-1. The suspensions were cast into a polystyrene mold and left to gel covered with Parafilm and kept at room temperature for 2 days. Gelation occurred within 20 min yielding free-standing films with thickness (t) value of 440 ± 10 μm. The samples were dried at 50 °C for 1 week. Elemental analyses for Si and Eu^{3+} were performed for M4-m-2 and M4-m-3 hybrids and the obtained values % (w/w), were: M4-m-2 (Si, 10.6; Eu^{3+}, 4.4) and M4-m-3 (Si, 10.6; Eu^{3+}, 3.0). The hybrids are thermally stable until 100 °C (Figure S1 in the Supporting Information). For M4-m-1, the TGA curves remains unchanged between 100 and 350 °C, whereas for M4-m-2 and M4-m-3, a weight loss decrease of 42% and 45%, respectively, was detected in the range 100−550 °C, corresponding to the decomposition of the tta.[50]

Synthesis and Preparation of the Thin Films Based on M4-m-2 by Spin-Coating. Borosilicate substrates (Normax microslides, 25 × 25 mm^2) were cleaned with acetone, immersed in a mixture of hydrogen peroxide and sulfuric acid (piranha solution), and then rinsed and stored in distilled H_2O. Prior to coating, they were dried by spin-coating (5000 rpm, 50 s), treated with MeOH, and dried again by spin-coating immediately prior to use. The thin films, sequentially designed from F1 to F25, were prepared based on different conditions, such as concentration of the precursor, spinning speed, aging time prior to coating, and solvent type (Table S1 in Supporting Information). $EuCl_3 \cdot 6H_2O$ (3.55 mg), tta−H (4.3 mg), and H_2O (5 μL) were incorporated into a suspension of P4-m (30 or 90 or 120 mg) dissolved in 1.30, 1.26, 1.25, and 1.25 mL of EtOH, MeOH, 1-PrOH, and DMF:MeOH = 1:5.5 molar ratio, respectively. The mixture was stirred for 20 min at room temperature, leading to a clear solution, then 0.1 M NH_4F (0.5 μL) was added. The final weight concentrations of P4-m were 3.0, 9.0, and 12.0 wt %. The substrates were held by suction on a chuck, which was placed on the axis of the spin coater (SCS Specialty Coating Systems, spin-coat G3−8). The thin films were prepared by spin-coating using two drops of the sol (with variable aging time prior to coating: 1, 4, 8, 11, and 14 min) on the glass substrates, with an acceleration time of 10 s and a spin time of 50 s, and at a spin rate of 1000, 2000, or 5000 rpm. They were finally dried at 70 °C overnight.

Elemental Analysis. Elemental analysis for Eu and Si were performed by inductively coupled plasma optical emission spectroscopy (ICP-OES) analysis on a Jobin Yvon Activa-M instrument with a glass concentric nebulizer. For the Eu analysis the samples were digested under microwaves with 0.5 mL of hydrochloric acid (HCl) and 1 mL of nitric acid (HNO_3). For the Si analysis the samples were digested under microwaves with 1 mL of nitric acid (HNO_3) and 0.5 mL of hydrofluoric acid (HF). After being digested under microwaves, the samples were recovered in 50 mL of ultrapure water. The method is accurate within 10%.

Fourier Transform Infrared (FT-IR) Spectroscopy. Middle-infrared experiments (400−5000 cm^{-1}) were recorded both in the transmission and attenuated total reflectance (ATR) mode. The measurements were carried out on a Bruker IFS 66 V spectrometer under vacuum equipped with a N_2-cooled mercury cadmium telluride (MCT) detector, a Globar source, and potassium bromide (KBr) beam splitter. The spectral resolution was 4 cm^{-1}, and 64 scans were coadded for each spectrum. In transmission, KBr pellets (0.8 mg sample/300 mg KBr) were prepared under 8 tons pressure. Prior to record the spectra, the pellets were dried at 100 °C for about 20 h, in order to reduce the levels of adsorbed water. Far-infrared (30−400 cm^{-1}) experiments were recorded in the transmission mode using a liquid He-cooled bolometer, Hg arc discharge source and mylar 6 μm beam splitter coated with germanium. Polyethylene pellets (3 mg sample/70 mg polyethylene) were prepared. The tta-H concentration was increased up to 5.5 mg to be able to discriminate its vibrational signatures.

UV−visible Absorption. UV−visible absorption spectra were measured using a dual-beam spectrometer Lambda 950, (PerkinElm-er) with a 150 mm diameter Spectralon integrating sphere, over the scan range 250−800 nm and a resolution of 1.0 nm. The spin-coating films the region below 300 nm was not assessed due to the glass substrate high absorbance. The absorption coefficient (α, cm^{-1}) was estimated using the Lambert−Beer equation (α = Abs/t, where Abs is the absorbance and t the thickness). Photoluminescence. The photoluminescence spectra were recorded at room temperature with a modular double grating excitation spectrofluorimeter with a TRIAX 320 emission monochromator (Fluorolog-3, Horiba Scientific) coupled to a R928 Hamamatsu photomultiplier, using a front face acquisition mode. The excitation source was a 450 W xenon (Xe) arc lamp. The emission spectra were corrected for detection and optical spectral response of the spectrofluorimeter and the excitation spectra were corrected for the spectral distribution of the lamp intensity using a photodiode reference detector. The emission decay curves were measured with the setup described for the luminescence spectra using a pulsed Xe−Hg lamp (6 μs pulse at half width and 20−30 μs tail).

Absolute Emission Quantum Yields. The absolute emission quantum yields (q) were measured at room temperature using a quantum yield measurement system C9920−02 from Hamamatsu with a 150 W xenon lamp coupled to a monochromator for wavelength discrimination, an integrating sphere as sample chamber and a multichannel analyzer for signal detection. Three measurements were made for each sample so that the average value is reported. The method is accurate to within 10%.

Profilometry. A TENCOR Alpha-Step IQ profilometer was used to measure the thickness t of the films. The method is accurate to within 0.1%.

Ellipsometry. The spectroscopic ellipsometry measurements were made using an AutoSE ellipsometer (Horiba Scientific) with a total of 250 points in the wavelength interval of 440−800 nm, an incidence angle of 70°, an acquisition time of 22 ms per point, and an average of 10 measurements per point. The refractive index dispersion curve was calculated using the Lorentz model detailed elsewhere.[51,52]

Optical Conversion Efficiency. The optical power at the LSCs output was estimated using a commercial photodiode (IF D91, Industrial Fiber Optics, Inc.) with wall-plug efficiency to the AM1.5G solar spectrum distribution of 4%. All measurements were performed under AM1.5G illumination (at 1000 W m^{-2}) using a 150 W xenon arc lamp class A solar simulator (Abet Technologies model 10500).

■ RESULTS AND DISCUSSION

Scanning electronic microscopy and ^{29}Si and ^{13}C solid-state NMR are used to characterize the structure of the powdered M4-m-2 and M4-m-3 xerogels (Figures S2−S4 in Supporting Information). No tta−H related signal (115−185 ppm) is observed in the ^{13}C solid-state NMR, probably due to the paramagnetic character of the Eu^{3+} ions bonded to this ligand. To demonstrate the presence of these ligands, and to gain better insights into the local structure, we performed an in-depth analysis by vibrational spectroscopies.

Middle, far-infrared,[53,54] and Raman[55] spectroscopies are known to be very powerful techniques to sign the presence of H bonding. Noncovalent interactions involving amide groups in hybrid silica, and in particular H-bonding,[56] are probed in the intramolecular frequency range from 1500−1750 cm^{-1} (Amide I and Amide II vibrations) and 3000−3700 cm^{-1} (Amide A vibrations). The infrared active Amide I band profile, dominated by carbonyl stretching vibrations ν(CO) around 1673 cm^{-1} (M4-m-4, see the Supporting Information), is significantly modified after doping (Figure S5a in the Supporting Information). As expected,[48] a new contribution appears for M4-m-1 at lower frequency around 1650 cm^{-1} featuring the ligand interaction between Eu^{3+} ions and carbonyl groups. Amide II infrared vibrations, arising mainly from NH in-plane bending, appear to be insensitive to the doping. As the Amide I band is splitted between unengaged (1673 cm^{-1}) and

engaged C=O (1650 cm^{-1}) in the ligand interaction, complexation seems to involve mainly one part of the carbonyl pairs. The same conclusions are derived from Raman spectroscopy (Figure S5b in the Supporting Information).

Superimposition of the vibrational results obtained for M4-m-1, M4-m-2, Eu(tta)$_3$(H$_2$O)$_2$, and tta-H are show in Figure S6 and S7 in Supporting Information. At first glance, M4-m-2 appears to be dominated by the combination of the spectra of Eu(tta)$_3$(H$_2$O)$_2$ and M4-m-1. Yet, our results show that some tta-H ligand molecules remain uncomplexed as tta-H vibrational feature at 1110 cm^{-1} is observed in M4-m-2 (see arrow in Figure S6a in Supporting Information). Besides, the deconvolution of the Amide I band (Figure 1) evidence a
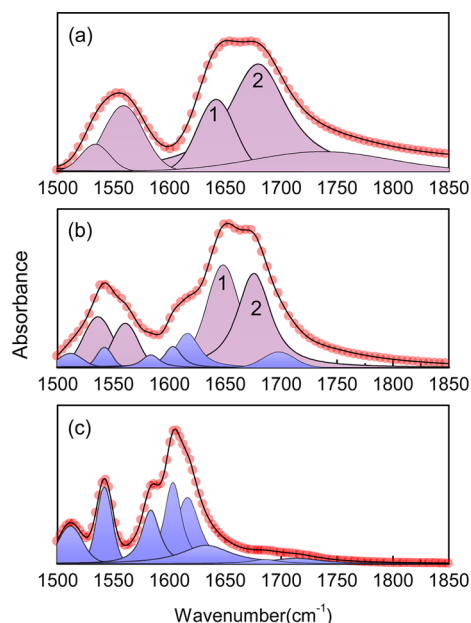

Figure 1. Infrared spectra in the region of the Amide I and Amide II vibrations of (a) M4-m-1, (b) M4-m-2, and (c) Eu(tta)$_3$ (H$_2$O)$_2$. The deconvolution using a sum of Gaussian functions (shadowed areas) and the overall fit (red circles) are also shown.

broader dispersion of Amide I vibrations in M4-m-1, as compared to M4-m-2. The relative intensity and positions between the most engaged ν(CO) (component 1) and the less engaged ν(CO) (component 2) are deeply modified after tta–H incorporation. The main Amide I (component 2) appears more intense, broader and blue-shifted for M4-m-1, indicating that supramolecular interactions around carbonyl due to the complexation with Eu^{3+} are increased for M4-m-2. Therefore, this trend indicates a deep modification of the ligand environment due to the presence of tta–H around Eu^{3+}. M4-m-2 cannot be considered as a simple physical mixture between M4-m-1 and Eu(tta)$_3$(H$_2$O)$_2$.

Specific Eu^{3+}–ligand vibrational features can be probed in the far-infrared domain below 300 cm^{-1}.[57,58] Figure 2 shows far-infrared absorption spectra comparing M4-m-2, Eu-(tta)$_3$(H$_2$O)$_2$, and tta-H ligand. The far-infrared spectrum of M4-m-2 is dominated by a significant feature around 177 cm^{-1} (labeled IB), superimposed with a broad continuum of H bonded water vibrations, in agreement with the vibrational contribution exhibited on M4-m-1 spectrum (Figure S8 in the Supporting Information). The infrared spectrum of Eu-(tta)$_3$(H$_2$O)$_2$ gives insight concerning the origin of this IB
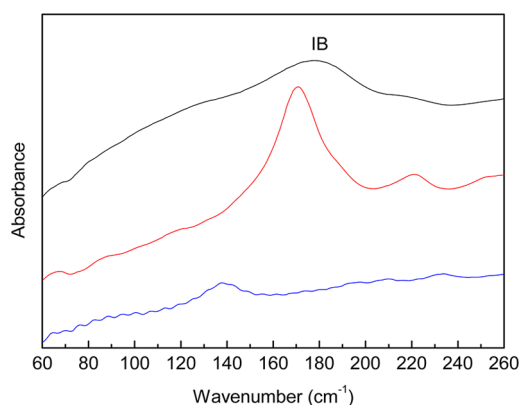

Figure 2. Far-infrared spectra of M4-m-2 (black line), Eu(tta)$_3$(H$_2$O)$_2$ (red line), and tta−H (blue line).

band. Indeed, an intense sharp feature around 170 cm^{-1} is seen for Eu(tta)$_3$(H$_2$O)$_2$ relative to tta−H ligand. We assume therefore that IB signs the interaction of Eu^{3+} with complexed tta and H$_2$O molecules. In agreement with this assumption, the temperature dependence of this band is anharmonic (around +5 cm^{-1}), as expected for an external mode,[59] whereas internal features are quasi harmonic (Figure S9 in Supporting Information). Besides, for M4-m-2, IB band is up-shifted (+7 cm^{-1}), compared to Eu(tta)$_3$(H$_2$O)$_2$. A strengthening of the complexation efficiency is therefore suggested for M4-m-2, compared to M4-m-1, in agreement with the results in the middle-infrared. Thus, our results suggest a cooperative effect of malonamide and tta−H to complex Eu^{3+} ions.

Furthermore, the decrease in intensity of the HBH$_2$O (intermolecular H bonding between H$_2$O molecules) contribution for M4-m-2 (Figure S8 in Supporting Information) suggests that the number of Eu^{3+}-coordinated water molecules decreases, compared to M4-m-1.

Figure 3 compares the room-temperature emission spectra of M4-m-1, M4-m-2, and M4-m-3 excited at the wavelength that maximized the emission intensity. The emission spectra of M4-m-2 and M4-m-3 are formed by a series of straight lines ascribed to the Eu^{3+} $^5D_0 \rightarrow {}^7F_{0-4}$ transitions. Independently of the selected excitation wavelengths (270−464 nm), no sign of the M4-m-4 intrinsic emission (Figure S10 in the Supporting Information) could be observed, which readily suggests efficient hybrid-to-ligand and/or hybrid−to−Eu^{3+} energy transfer.[60] The emission spectrum of M4-m-1 displays the intra-4f^6 lines overlapped with a broad emission (350−550 nm) assigned to the hybrid host (inset in Figure 3a). Changes in the Eu^{3+} coordination sphere resulting from the addition of the tta ligand can be inferred from the analysis of the relative intensity of the intra-4f^6 transitions for M4-m-1, M4-m-2 and M4-m-3. It is clear that the relative intensity of the $^5D_0 \rightarrow {}^7F_{1,4}$ transitions significantly decreases after the tta-H incorporation. In fact, the integrated intensity ratios I_{02}/I_{04} and I_{02}/I_{01} (I_{0J}, $J = 1$, 2 and 4, represents the integrated intensity of the $^5D_0 \rightarrow {}^7F_{1,2,4}$ transitions) strongly depend on the presence of tta ligand, in particular I_{02}/I_{04} and I_{02}/I_{01} increases from 1.6 and 3.4 (M4-m-1) to 6.6/6.5 and 11.7/13.5 (M4-m-2/M4-m-3). Moreover, the similarity between the intensity ratios for M4-m-2 and M4-m-3 suggests an analogous Eu^{3+} local coordination. Therefore, the larger concentration of tta ligands in M4-m-3, compared to that in M4-m-2, leads to the presence of free (noncoordinated) tta ligands, as detected in the FTIR and Raman studies. We will come back to this point.
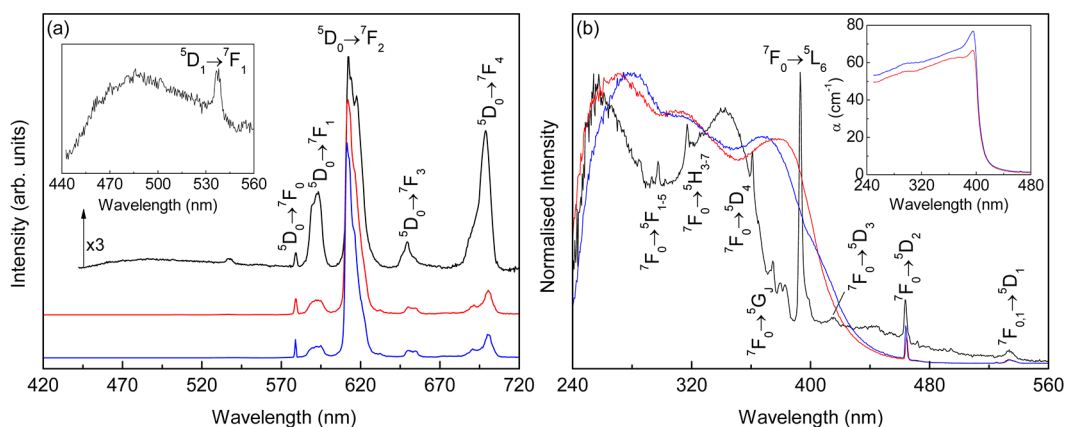
Figure 3. (a) Emission spectra of M4-m-1 (black line) excited at 393 nm and of M4-m-2 (red line) and M4-m-3 (blue line) excited at 380 nm and (b) excitation spectra monitored at 612 nm. The insets in a and b show a magnification of the emission spectrum ($\times$ 3) of M4-m-1 and the UV$-$vis absorption coefficients of M4-m-2 and M4-m-3, respectively.
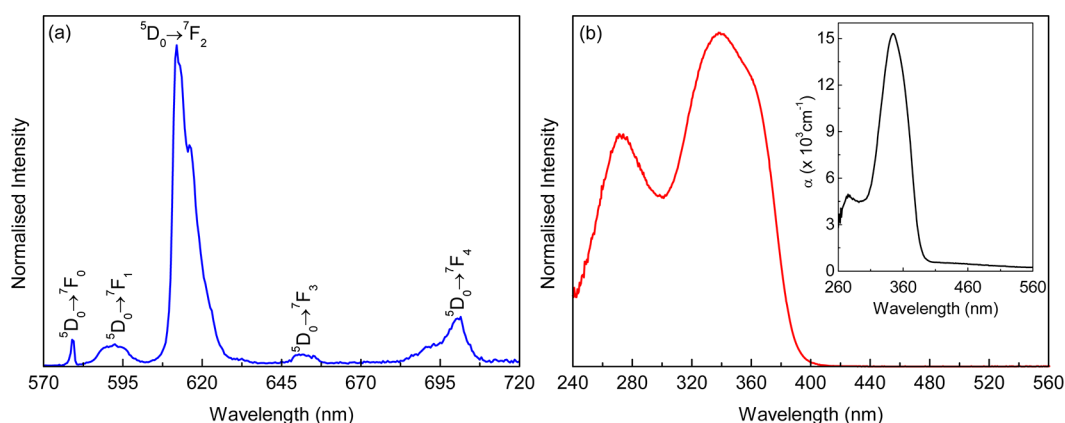

Figure 4. (a) Emission and (b) excitation spectra of F6 excited at 380 nm and monitored at 612 nm, respectively. The inset shows the UV$-$vis absorption coefficient.

The excitation spectra of M4-m-2 and M4-m-3 were monitored around the $^5D_0 \rightarrow {}^7F_2$ transition (Figure 3b) showing three main components peaking at 270/280, 320, and 380 nm and two low-relative-intensity intra-$4f^6$ transitions. The relatively low intensity of the intra-$4f^6$ lines indicates that the Eu^{3+} excited states in M4-m-2 and M4-m-3 are mainly populated via ligand-sensitization. The high-wavelength components at 320 and 380 nm resemble those already observed for isolated Eu(tta)$_3$(H$_2$O)$_2$[61] and for organic$-$inorganic hybrids incorporating Eu(tta)$_3$(H$_2$O)$_2$ and Eu(tta)$_3$phen (phen = 1,10-phenanthroline), being ascribed to the $\pi-\pi^*$ electronic transition of the organic ligands.[62] We should note that the hybrid intrinsic excited states also contribute for the excitation spectra. This conclusion is derived from the analysis of the excitation spectra of M4-m-4 and M4-m-1 monitored along the hybrid host emission (Figures S10 and S11 and in the Supporting Information) that reveal a broad band with two components at 280 and 320 nm. Moreover, these two components are also present in the excitation spectrum of M4-m-1 monitored at 612 nm. For this hybrid the relative intensity of the intra-$4f^6$ lines is higher than that of the hybrid-related components indicating that the Eu^{3+} sensitization occurs essentially through direct intra-$4f^6$ excitation. Apart from changes in the relative intensity, the UV$-$visible absorption spectrum (inset Figure 3b) reveals the same components already detected in the excitation spectra.

Moreover, an increase in the maximum absorption coefficient (α) at 395 nm from 67 to 77 cm^{-1} is observed as the tta ligand amount increases from M4-m-2 to M4-m-3.

The $^5D_0$ emission decay curves were monitored under direct intra-$4f^6$ excitation (393 nm, $^5L_6$, and 465 nm, $^5D_2$) revealing a single exponential behavior (Figure S12 in the Supporting Information). From the data best fit, $^5D_0$ lifetime values of 0.266 $\pm$ 0.002 ms (M4-m-1), 0.395 $\pm$ 0.002 ms (M4-m-2) and 0.392 $\pm$ 0.002 ms (M4-m-3) were found. The higher values found in the presence of tta-H are in good agreement with the ligand coordination to the Eu^{3+} ions in M4-m-2 and M4-m-3. Moreover, the identical values measured for M4-m-2 and M4-m-3 reinforces that the Eu^{3+} local coordination is similar in both hybrids, and therefore independent of the tta ligand concentration (as suggested above).

The $^5D_0$ lifetime values of M4-m-2 (0.47 $\pm$ 0.01 ms) and M4-m-3 (0.52 $\pm$ 0.01 ms) excited at 380 nm are larger than the value reported for Eu(tta)$_3$(H$_2$O)$_2$ (0.190 ms) excited at 389 nm,[63] which clearly points to minimization of radiationless deactivation in a coordination environment devoid of water molecules.[50] To further confirm it, the $^5D_0$ radiative (A_r) and nonradiative (A_{nr}) transition probabilities and the $^5D_0$ quantum efficiency (η) and the number of water molecules (n_w) were determined following a methodology described in detailed elsewhere[64] (see also the Supporting Information). For M4-m-2/M4-m-3 analogous values of η (32/31%), A_r (0.846/0.802

Table 1. Concentration of Precursor in Solvent (%), Spinning Rotation (rpm), Aging Time Prior to Coating (min), Thickness (t, nm), Maximum Absorption Coefficient (α, cm^{-1}), Absolute Emission Quantum Yield (q) at Distinct Excitation Wavelengths (λ_{exc}, nm), and n_{opt} (%) of Selected Films

films	concentration of precursor	spinning speed	aging time	thickness^a (σ)	α	q (λ_{exc} (nm))	n_{opt}
F1	3	1000	1	430 (5.8)	1158	0.60 ± 0.06 (345)	
F2			4			0.39 ± 0.04 (345)	
F3			8			0.31 ± 0.03 (365)	
F4			14	100 (19.2)	3466	0.30 ± 0.03 (365)	
F5	9	2000	1	90 (9.3)	45043	0.23 ± 0.02 (345)	12.3^b
							0.43^c
F6		5000	11	201 (2.6)	15294	0.21 ± 0.02 (365)	11.0^b
							0.38^c
F7	12	1000	1	375 (25)	20239	0.36 ± 0.04 (365)	6.4^b
							0.22^c

^{a}Values measured by profilometry, σ is the standard deviation. $^b\eta_{opt}$ calculated considering the solar irradiance in the absorbed region (53 W m^{-2}). $^c\eta_{opt}$ calculated considering the total solar irradiance (1000 W m^{-2}).

ms^{-1}), A_{nr} (1.686/1.749 ms^{-1}), and identical n$_w$ = 1.5 ± 0.1 was calculated, reinforcing the similarity of the Eu^{3+} local coordination sites in both hybrids. Maximum q values of 0.22 ± 0.02 and 0.34 ± 0.03 (excited at 320 nm) were measured for M4-m-2 and M4-m-3, respectively (Table S2 in the Supporting Information). Lower values (0.12 ± 0.01) were measured at higher excitation wavelengths (400 nm). Independently of the selected excitation wavelength, significantly lower values were measured in the absence of the tta ligand (M4-m-1), q = 0.02 ± 0.01, excited within 260−393 nm.

Featuring applications in the field of LSCs, the M4-m-2 hybrids were processed as thin films (by spin-coating) because when compared with the M4-m-3 systems they combine similar quantum yield at higher excitation wavelengths with lower incorporation of tta ligand. The role of the P4-m precursor concentration, the aging time of the solution to be deposited, the spinning conditions and the solvent were varied aiming at optimizing the optical properties of the films (Table S1 in the Supporting Information). On the basis of the higher emission quantum yield, seven films were selected to be tested as LSCs.

Apart from minor differences in the energy and relative intensity, the excitation and emission spectra are independent of the processing conditions (Figure 4 and Figure S13 in the Supporting Information). The emission spectrum of F6 (Figure 4a) is composed of the $^5D_0 \rightarrow {}^7F_{0-4}$ transitions, whose energy and relative intensity (I_{02}/I_{01} and I_{02}/I_{04} of 11.9 and 4.4, respectively) are closer to those of M4-m-2 (I_{02}/I_{04} and I_{02}/I_{01} of 11.7 and 6.6, respectively). The excitation spectrum of F6, monitored within the $^5D_0 \rightarrow {}^7F_2$ transition (Figure 4b), shows the presence of the hybrid intrinsic excited states (270 nm) and the organic ligands-related states (320 and 380 nm) that are blue-shifted when compared with that found in M4-m-2. This blue shift, also detected in the UV−visible absorption spectrum (Figure 4c), was already reported for analogous hybrids, being ascribed to the distinct gelification and condensation rates of the spin-coated thin films.[28] The maximum absorption coefficient values ($\sim 10^4$ cm^{-1}) are of the same order of magnitude as those measured for Eu^{3+}-containing urea-bipyridine bridged organosilanes.[28] The $^5D_0$ emission decay curves were monitored at 612 nm and excited at 360 nm. The $^5D_0$ lifetime values are approximately independent of the deposition conditions, except for F4 and F7 (Table S3 in the Supporting Information).

Despite analogous steady-state photoluminescence and lifetime values, q is strongly affected by the preparation

conditions. The highest q value (0.60 ± 0.06) was measured for F1 under excitation of 345 nm (Table 1 and Table S1 in the Supporting Information).

The photograph in Figure 5 illustrates the potential of the films to be used as LSCs because under AM1.5 illumination the
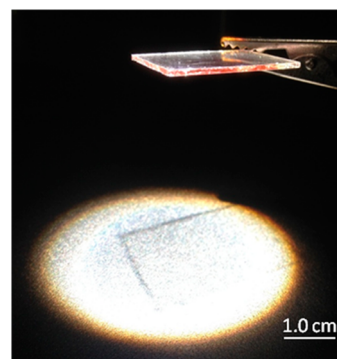

Figure 5. Photo of F6 under AM1.5G illumination.

light emitted at the surface is guided and concentrated at the substrate edges, where it can be collected by a PV cell.

The performance of the films as LSCs was quantified through the measurement of η_{opt} under AM1.5G illumination. The η_{opt} is given by the ratio between the power of the photodiode attached to the LSC (P_{out}) and the power of the photodiode exposed directly to the solar radiation (P_{in})[38]

$$\eta_{opt} = \frac{P_{out}}{P_{in}} = \frac{I_{sc}^L V_0^L}{I_{sc} V_0} \frac{1}{G} \frac{\eta_{solar}}{\eta_{PV}} \frac{\int I_{AM1.5G}(\lambda) d\lambda}{\int_{\lambda_1}^{\lambda_2} I_{AM1.5G}(\lambda) d\lambda} \tag{1}$$

where I_{SC}^L and V_0^L represent the short-circuit current and the open voltage when the photodiode is coupled to the LSC (I_{sc} and V_0 are the corresponding values of the photodiode exposed directly to the solar radiation), $G = A_s/A_e$ is the ratio between the surface area (A_s) and the area of the plate edges (A_e), η_{solar} is the efficiency of the photodiode relatively to the total solar spectrum and η_{PV} is the efficiency of the photodiode at the LSC emission wavelengths. The ratio

$$\frac{\eta_{solar}}{\eta_{PV}} = \frac{\int EQE_{device}(\lambda) I_{AM1.5G}(\lambda) d\lambda}{\int EQE_{PD}(\lambda) I_{AM1.5G}(\lambda) d\lambda} = 1.15 \tag{2}$$

where EQE_{device} and EQE_{PD} are the external quantum efficiencies of the LSC coupled to photodiode and of the photodiode, respectively. We note that despite the photodiode is coupled to a single edge, G is calculated considering A_e as the area of the four extremities, as the same light concentration is expected at each LSC end. The n_{opt} values were calculated considering the fraction of absorbed photons (53 W m^{-2}) and the total solar spectral irradiance (1000 W m^{-2}). Concerning the mismatch in the UV spectral region between the AM1.5G solar irradiance and that of the Xe lamp of the solar simulator used (Figure S14 in the Supporting Information), $I_{AM1.5G}$ in eq 2 is replaced by the emission spectrum of the solar simulator, $\eta_{solar}/\eta_{PV} = 0.9$, yielding η_{opt} values listed in Table 1. As far as we are concerned, these are the first η_{opt} measured under AM1.5 illumination for Ln^{3+}-based LSC. Thus, the performance of the F5, F6, and F7-based LSCs is compared with the figures of merit known for planar single-layer LSCs, whose optically active centers are QDs[42−44] and dyes.[39−42] We note that as distinct definitions and experimental conditions may be employed to estimate η_{opt}, the comparison will be performed using the figure of merit calculated using eq 1, or an identical definition, under AM1.5G solar illumination. Examples involving illumination using other standard conditions (e.g., diffuse cloudy day indoor illumination[65]) or η_{opt} measured at a particular excitation wavelength[28,35,47,48] are not consider. The maximum η_{opt} value here reported calculated using the fraction of absorbed photons (12.3% for F5) is of the same order of magnitude of LSCs based on CdSe/CdS QDs incorporated in poly(methyl methacrylate) (PMMA) (10.2%)[43] and LSCs using red305-doped PMMA (16.3%).[39] In the case of η_{opt} values calculated considering the total number of incident photons, the highest value measured for F5 (0.43%) is similar to that found for CdSe and ZnS QDs in toluene (0.3%)[42] being, however, 1 order of magnitude smaller than the η_{opt} of LSCs containing PbS QDs (1.4%),[44] Rhodamine B (2.6%),[42] and RedF (3.4%)[42] in toluene and PMMA codoped with LumogenF and Red305 (2.8%).[41]

We note that F5 and F6 reveal similar η_{opt} values, whereas for F7 a lower value was found. Aiming at further interpret the differences in the measured η_{opt} values, spectroscopic ellipsometry was used to characterize the dispersion curves for F6 and F7 (Figure 6 and Figure S15 in the Supporting Information), enabling the determination of the trapping efficiency, $\eta_{trap} = (1 - 1/n_p^2)^{1/2}$, where n_p is the refractive index of the emitting medium at the emission wavelength (612

nm). The η_{trap} defines the fraction of photons confined within the substrate. The refractive index values of F6 are higher than those of F7 reinforcing the role of the deposition conditions on this optical parameter, as recently highlighted for analogous hybrid materials.[35] The calculated thicknesses are $t = 205.0 \pm 4.8$ nm (F6) and $t = 407.0 \pm 3.3$ nm (F7), which are in good agreement with the complementary profilometry studies (Table 1), suggesting that the modeling of the ellipsometric data yielded realistic parameters. Despite the larger refractive index of F6 (1.525) at the Eu^{3+} maximum emitting wavelength (612 nm) compared with that of F7 (1.489) an analogous $\eta_{trap} = 75\%$ is calculated for the LSCs based on F6 and F7. Therefore, we suggest that the larger thickness of the optical active layer in F7 may induce larger transport losses because of the scattering of the emitted light in the film[28] explaining the lower η_{opt} value relatively to F5 and F6.

CONCLUSIONS

In this work, the synthesis of the new ethane tetracarboxamide-based organosilane (P4-m) and its hydrolysis−condensation under nucleophilic catalysis in the presence of Eu^{3+} with and without tta−H have been achieved. Specific Eu^{3+} local coordination in M4-m-2 (with tta-H) compared to M4-m-1 (tta-H free) is suggested from vibrational and photoluminescence results. A Eu^{3+} cooperative complexation by tta−H and hybrids lead to a very significant increase of q. In addition, M4-m-2 was processed as thin films by spin-coating on glass substrates, where the P4-m concentration, aging time, spinning conditions and solvent type were varied to optimize the optical properties. Films with q value of 0.60 ± 0.06 excited at 345 nm and η_{opt} of 12.3% in the absorbing spectral region of the active layer (300−380 nm) were produced. These are the first quantitative reports for Ln^{3+}−LSCs providing evidence of the potential of Ln^{3+}-based hybrid coatings in the development of LSC prototypes.

ASSOCIATED CONTENT

⑤ Supporting Information

Experimental section, Figure S1−S15, and Table S1−S3. This material is available free of charge via the Internet at http://pubs.acs.org.

AUTHOR INFORMATION

Corresponding Authors
*E-mail: Jean-Louis.Bantignies@univ-montp2.fr.
*E-mail: lcarlos@ua.pt.

Notes
The authors declare no competing financial interest.

ACKNOWLEDGMENTS

Figure 6. Refractive index dispersion curves of F6 and F7.

■ REFERENCES

(1) Carlos, L. D.; Ferreira, R. A. S.; de Zea Bermudez, V.; Ribeiro, S. J. L. Lanthanide-Containing Light-Emitting Organic-Inorganic Hybrids: A Bet on the Future. *Adv. Mater.* **2009**, *21*, 509−534.

(2) Bunzli, J. C. G. Lanthanide Luminescence for Biomedical Analyses and Imaging. *Chem. Rev.* **2010**, *110*, 2729−2755.

(3) Armelao, L.; Quici, S.; Barigelletti, F.; Accorsi, G.; Bottaro, G.; Cavazzini, M.; Tondello, E. Design of Luminescent Lanthanide Complexes: From Molecules to Highly Efficient Photo-Emitting Materials. *Coord. Chem. Rev.* **2010**, *254*, 487−505.

(4) Bünzli, J. C. G.; Eliseeva, S. V. Intriguing aspects of Lanthanide Luminescence. *Chem. Sci.* **2013**, *4*, 1939−1949.

(5) Sun, L. D.; Wang, Y. F.; Yan, C. H. Paradigms and Challenges for Bioapplication of Rare Earth Upconversion Luminescent Nanoparticles: Small Size and Tunable Emission/Excitation Spectra. *Acc. Chem. Res.* **2014**, *47*, 1001−1009.

(6) Brites, C. D. S.; Lima, P. P.; Silva, N. J. O.; Millán, A.; Amaral, V. S.; Palacio, F.; Carlos, L. D. A Luminescent Molecular Thermometer for Long-Term Absolute Temperature Measurements at the Nanoscale. *Adv. Mater.* **2010**, *22*, 4499−4504.

(7) Huang, X.; Han, S.; Huang, W.; Liu, X. Enhancing Solar Cell Efficiency: the Search for Luminescent Materials as Spectral Converters. *Chem. Soc. Rev.* **2013**, *42*, 173−201.

(8) Chen, G. Y.; Yang, C. H.; Prasad, P. N. Nanophotonics and Nanochemistry: Controlling the Excitation Dynamics for Frequency Up- and Down-Conversion in Lanthanide-Doped Nanoparticles. *Acc. Chem. Res.* **2013**, *46*, 1474−1486.

(9) Gai, S. L.; Li, C. X.; Yang, P. P.; Lin, J. Recent Progress in Rare Earth Micro/Nanocrystals: Soft Chemical Synthesis, Luminescent Properties, and Biomedical Applications. *Chem. Rev.* **2014**, *114*, 2343−2389.

(10) Sabbatini, N.; Guardigli, M.; Lehn, J. M. Luminescent Lanthanide Complexes as Photochemical Supramolecular Devices. *Coordin. Chem. Rev.* **1993**, *123*, 201−228.

(11) Binnemans, K., Rare Earth Beta-Diketonates. In *Handbook on the Physics and Chemistry of Rare Earths*, Gschneidner Jr., K. A.; Bünzli, J.-C. G.; Pecharsky, V. K., Eds. Elsevier: Amsterdam, 2005; Vol. 35, pp 107−272.

(12) Lima, P. P.; Nolasco, M. M.; Paz, F. A. A.; Ferreira, R. A. S.; Longo, R. L.; Malta, O. L.; Carlos, L. D. Photo-click Chemistry to Design Highly Efficient Lanthanide Beta-Diketonate Complexes Stable under UV Irradiation. *Chem. Mater.* **2013**, *25*, 586−598.

(13) Yan, B. Recent Progress in Photofunctional Lanthanide Hybrid Materials. *RSC Adv.* **2012**, *2*, 9304−9324.

(14) Escribano, P.; Julián-López, B.; Planelles-Aragó, J.; Cordoncillo, E.; Viana, B.; Sanchez, C. Photonic and Nanobiophotonic Properties of Luminescent Lanthanide-doped Hybrid Organic-Inorganic Materials. *J. Mater. Chem.* **2008**, *18*, 23−40.

(15) Binnemans, K. Lanthanide-Based Luminescent Hybrid Materials. *Chem. Rev.* **2009**, *109*, 4283−4374.

(16) Carlos, L. D.; Ferreira, R. A. S.; de Zea Bermudez, V.; Julián-López, B.; Escribano, P. Progress on Lanthanide-based Organic-Inorganic Hybrid Phosphors. *Chem. Soc. Rev.* **2011**, *40*, 536−549.

(17) Feng, J.; Zhang, H. Hybrid Materials Based on Lanthanide Organic Complexes: A Review. *Chem. Soc. Rev.* **2013**, *42*, 387−410.

(18) Wang, Y. G.; Lin, N. N. Highly Transparent and Luminescent Lanthanide Ion-Containing Bridged Polysilsesquioxanes. *Photoch. Photobio. Sci.* **2011**, *10*, 42−47.

(19) Kwak, S. Y.; Yang, S.; Kim, N. R.; Kim, J. H.; Bae, B. S. Thermally Stable, Dye-Bridged Nanohybrid-Based White Light-Emitting Diodes. *Adv. Mater.* **2011**, *23*, 5767−5772.

(20) Zhang, Y.; Wei, W.; Das, G. K.; Tan, T. T. Y. Engineering Lanthanide-based Materials for Nanomedicine. *J. Photochem. Photobio. C* **2014**, *20*, 71−96.

(21) Machida, K.; Li, H.; Ueda, D.; Inoue, S.; Adachi, G. Preparation and Application of Lanthanide Complex Incorporated Ormosil Composite Phosphor Films. *J. Lumin.* **2000**, *87−9*, 1257−1259.

(22) Wilson, L. R.; Richards, B. S. Measurement Method for Photoluminescent Quantum Yields of Fluorescent Organic Dyes in Polymethyl Methacrylate for Luminescent Solar Concentrators. *Appl. Opt.* **2009**, *48*, 212−220.

(23) Moudam, O.; Rowan, B. C.; Alamiry, M.; Richardson, P.; Richards, B. S.; Jones, A. C.; Robertson, N. Europium Complexes with high total Photoluminescence Quantum Yields in solution and in PMMA. *Chem. Commun.* **2009**, 6649−6651.

(24) Wang, T. X.; Zhang, J.; Ma, W.; Luo, Y. H.; Wang, L. J.; Hu, Z. J.; Wu, W. X.; Wang, X.; Zou, G.; Zhang, Q. J. Luminescent Solar Concentrator employing Rare Earth Complex with Zero Self-Absorption Loss. *Sol. Energy* **2011**, *85*, 2571−2579.

(25) Correia, S. F. H.; de Zea Bermudez, V.; Ribeiro, S. J. L.; André, P. S.; Ferreira, R. A. S.; Carlos, L. D. Luminescent Solar Concentrators: Challenges for Lanthanide-based Organic−Inorganic Hybrid Materials. *J. Mater. Chem. A* **2014**, *2*, 5580−5596.

(26) Corriu, R. J. P.; Moreau, J. J. E.; Thépot, P.; Wong Chi Man, M. New Mixed Organic Inorganic Polymers - Hydrolysis and Polycondensation of Bis(Trimethoxysilyl)Organometallic Precursors. *Chem. Mater.* **1992**, *4*, 1217−1224.

(27) Shea, K. J.; Loy, D. A. Bridged Polysilsesquioxanes. Molecular-Engineered Hybrid Organic-Inorganic Materials. *Chem. Mater.* **2001**, *13*, 3306−3319.

(28) Graffion, J.; Cattoën, X.; Wong Chi Man, M.; Fernandes, V. R.; André, P. S.; Ferreira, R. A. S.; Carlos, L. D. Modulating the Photoluminescence of Bridged Silsesquioxanes incorporating Eu³⁺-Complexedn,n′-Diureido-2,2′-bipyridine Isomers: Application for Luminescent Solar Concentrators. *Chem. Mater.* **2011**, *23*, 4773−4782.

(29) Hatton, B. D.; Landskron, K.; Whitnall, W.; Perovic, D. D.; Ozin, G. A. Spin-Coated Periodic Mesoporous Organosilica Thin Films - Towards a New Generation of Low-Dielectric-Constant Materials. *Adv. Funct. Mater.* **2005**, *15*, 823−829.

(30) Karatchevtseva, I.; Cassidy, D. J.; Won Chi Man, M.; Mitchell, D. R. G.; Hanna, J. V.; Carcel, C.; Bied, C.; Moreau, J. J. E.; Bartlett, J. R. Structural Evolution of Self-assembling Nanohybrid thin Films from Functionalized Urea Precursors. *Adv. Funct. Mater.* **2007**, *17*, 3926−3932.

(31) Hu, S. W.; Xu, Y.; Jiang, D.; Wu, D.; Sun, Y. H.; Deng, F. Moisture-Resistant Protective Films for UV-light Filter based on Diisocyanate-Bridged Polysilsesquioxanes. *Thin Solid Films* **2009**, *518*, 348−354.

(32) Chamas, Z. E.; Guo, X. M.; Canet, J. L.; Gautier, A.; Boyer, D.; Mahiou, R. Clicked Dipicolinic Antennae for Lanthanide Luminescent Probes. *Dalton Trans.* **2010**, *39*, 7091−7097.

(33) Wang, Y.; Wang, Y.; Gan, Q. Synthesis and Luminescence Properties of Spherical Bridged Polysilsequioxanes Activated by Lanthanide Ions. *J. Sol-Gel Sci. Technol.* **2010**, *56*, 141−144.

(34) Wang, Y.; Wang, Y. G.; Cao, P. P.; Li, Y. N.; Li, H. R. Rectangular-Plate like Organosilica Microcrystals based on Silylated beta-Diketone and Lanthanide Ions. *CrystEngComm* **2011**, *13*, 177−181.

(35) Graffion, J.; Cojocariu, A. M.; Cattoën, X.; Ferreira, R. A. S.; Fernandes, V. R.; André, P. S.; Carlos, L. D.; Wong Chi Man, M.; Bartlett, J. R. Luminescent Coatings from Bipyridine-based Bridged Silsesquioxanes Containing Eu³⁺ and Tb³⁺ Salts. *J. Mater. Chem.* **2012**, *22*, 13279−13285.

(36) Bünzli, J.-C. G.; Chauvin, A.-S., Lanthanides in Solar Energy Conversion. In *Handbook on the Physics and Chemistry of Rare-Earths*, Bünzli, J.-C. G.; Pecharsky, V. K., Eds. Elsevier B. V.: Amsterdam, 2014; Vol. *44*, pp 169−282.

(37) Weber, W. H.; Lambe, J. Luminescent Greenhouse Collector for Solar Radiation. *Appl. Opt.* **1976**, *15*, 2299−2300.

(38) Reisfeld, R.; Shamrakov, D.; Jorgensen, C. Photostable Solar Concentrators Based on Fluorescent Glass-Films. *Sol. Energy Mater. Sol. C* **1994**, *33*, 417−427.

(39) Albers, P. T. M.; Bastiaansen, C. W. M.; Debije, M. G. Dual Waveguide Patterned Luminescent Solar Concentrators. *Sol. Energy* **2013**, *95*, 216−223.

(40) Wittwer, V.; Stahl, W.; Goetzberger, A. Fluorescent Planar Concentrators. *Sol. Energy Mater.* **1984**, *11*, 187−197.

(41) Griffini, G.; Levi, M.; Turri, S. Novel Crosslinked Host Matrices based on Fluorinated Polymers for Long-Term durability in Thin-film Luminescent Solar Concentrators. *Sol. Energy Mater. Sol. C* **2013**, *118*, 36−42.

(42) Sholin, V.; Olson, J. D.; Carter, S. A. Semiconducting Polymers and Quantum Dots in Luminescent Solar Concentrators for Solar Energy Harvesting. *J. Appl. Phys.* **2007**, *101*, 123114.

(43) Meinardi, F.; Colombo, A.; Velizhanin, K. A.; Simonutti, R.; Lorenzon, M.; Beverina, L.; Viswanatha, R.; Klimov, V. I.; Brovelli, S. Large-area Luminescent Solar Concentrators based on 'Stokes-shift-engineered' Nanocrystals in a Mass-polymerized PMMA Matrix. *Nat. Photonics* **2014**, *8*, 392−399.

(44) Shcherbatyuk, G. V.; Inman, R. H.; Wang, C.; Winston, R.; Ghosh, S. Viability of using Near Infrared PbS Quantum Dots as Active Materials in Luminescent Solar Concentrators. *Appl. Phys. Lett.* **2010**, *96*, 191901.

(45) Katsagounos, G.; Stathatos, E.; Arabatzis, N. B.; Keramidas, A. D.; Lianos, P. Enhanced Photon Harvesting in Silicon Multicrystalline Solar Cells by New Lanthanide Complexes as Light Concentrators. *J. Lumin.* **2011**, *131*, 1776−1781.

(46) Wang, X.; Wang, T.; Tian, X.; Wang, L.; Wu, W.; Luo, Y.; Zhang, Q. Europium Complex Doped Luminescent Solar Concentrators with Extended Absorption range from UV to Visible Region. *Sol. Energy* **2011**, *85*, 2179−2184.

(47) Misra, V.; Mishra, H. Photoinduced Proton Transfer Coupled with Energy Transfer: Mechanism of Sensitized Luminescence of Terbium ion by Salicylic Acid doped in Polymer. *J. Chem. Phys.* **2008**, *128*, 244701.

(48) Nolasco, M. M.; Vaz, P. M.; Freitas, V. T.; Lima, P. P.; André, P. S.; Ferreira, R. A. S.; Vaz, P. D.; Ribeiro-Claro, P.; Carlos, L. D. Engineering Highly Efficient Eu(III)-based Tri-ureasil Hybrids toward Luminescent Solar Concentrators. *J. Mater. Chem. A* **2013**, *1*, 7339−7350.

(49) Correia, S. F. H.; Lima, P. P.; André, P. S.; Ferreira, R. A. S.; Carlos, L. D. High-Efficiency Luminescent Solar Concentrators for Flexible Waveguiding Photovoltaics. *Sol. Energy Mater. Sol. Cells* **2015**, *138*, 51−57.

(50) Biju, S.; Eom, Y. K.; Bunzli, J.-C. G.; Kim, H. K. Biphenylene-Bridged Mesostructured Organosilica as a Novel Hybrid Host Material for Ln III (Ln = Eu, Gd, Tb, Er, Yb) Ions in the Presence of 2-Thenoyltrifluoroacetone. *J. Mater. Chem. C* **2013**, *1*, 3454−3466.

(51) Fernandes, V. R.; Vicente, C. M. S.; Wada, N.; André, P. S.; Ferreira, R. A. S. Multi-objective Genetic Algorithm Applied to Spectroscopic Ellipsometry of Organic-Inorganic Hybrid Planar Waveguides. *Opt. Express* **2010**, *18*, 16580−16586.

(52) Graffion, J.; Cattoën, X.; Freitas, V. T.; Ferreira, R. A. S.; Wong Chi Man, M.; Carlos, L. D. Engineering of Metal-Free Bipyridine-Based Bridged Silsesquioxanes for Sustainable Solid-State Lighting. *J. Mater. Chem.* **2012**, *22*, 671−6715.

(53) Bantignies, J. L.; Vellutini, L.; Sauvajol, J. L.; Maurin, D.; Wong Chi Man, M.; Dieudonné, P.; Moreau, J. J. E. Hydrogen Bonding in Self Organized Lamellar Hybrid Silica. *J. Non-Cryst. Solids* **2004**, *345*, 605−609.

(54) Creff, G.; Pichon, B. P.; Blanc, C.; Maurin, D.; Sauvajol, J. L.; Carcel, C.; Moreau, J. J. E.; Roy, P.; Bartlett, J. R.; Wong Chi Man, M.; Bantignies, J. L. Self-Assembly of Bridged Silsesquioxanes: Modulating Structural Evolution via Cooperative Covalent and Noncovalent Interactions. *Langmuir* **2013**, *29*, 5581−5588.

(55) Michel, T.; Alvarez, L.; Sauvajol, J. L.; Almairac, R.; Aznar, R.; Mathon, O.; Bantignies, J. L.; Flahaut, E. Structural Selective Charge transfer in Iodine-doped Carbon Nanotubes. *J. Phys. Chem. Solids* **2006**, *67*, 1190−1192.

(56) Dieudonné, P.; Wong Chi Man, M.; Pichon, B. P.; Vellutini, L.; Bantignies, J. L.; Blanc, C.; Creff, G.; Finet, S.; Sauvajol, J. L.; Bied, C.; Moreau, J. J. E. In situ X-ray Measurements to Probe a New Solid-State Polycondensation Mechanism for the Design of Supramolecular Organo-Bridged Silsesquioxanes. *Small* **2009**, *5*, 503−510.

(57) Clark, R. J. H.; Williams, C. S. Far-Infrared Spectra of Metal-Halide Complexes of Pyridine and Related Ligands. *Inorg. Chem.* **1965**, *4*, 350−357.

(58) Zolin, V. F.; Puntus, L. N.; Tsaryuk, V. I.; Kudryashova, V. A.; Legendziewicz, J.; Gawryszewska, P.; Szostak, R. Spectroscopy of Europium and Terbium Pyridine-Carboxylates. *J. Alloys Compd.* **2004**, *380*, 279−284.

(59) Le Parc, R.; Hermet, P. S. R.; Maurin, D.; Alvarez, L.; Ivanov, A.; Quimby, J. M.; Hanley, C. G.; Scott, L. T.; Bantignies, J.-L. New Insights on Vibrational Dynamics of Corannulene. *J. Phys. Chem. C* **2012**, *116*, 25089−25096.

(60) Lima, P. P.; Nobre, S. S.; Freire, R. O.; Alves Junior, S.; Ferreira, R. A. S.; Pischel, U.; Malta, O. L.; Carlos, L. D. Energy Transfer Mechanisms in Organic-Inorganic Hybrids incorporating Europium-(III): A Quantitative Assessment by Light Emission Spectroscopy. *J. Phys. Chem. C* **2007**, *111*, 17627−17634.

(61) Kai, J. A.; Felinto, M. C. F. C.; Nunes, L. A. O.; Malta, O. L.; Brito, H. F. Intermolecular Energy Transfer and Photostability of Luminescence-tuneable Multicolour PMMA Films doped with Lanthanide-beta-Diketonate Complexes. *J. Mater. Chem.* **2011**, *21*, 3796−3802.

(62) Fernandes, M.; de Zea Bermudez, V.; Ferreira, R. A. S.; Carlos, L. D.; Charas, A.; Morgado, J.; Silva, M. M.; Smith, M. J. Highly Photostable Luminescent Poly (e-caprolactone) Siloxane Biohybrids Doped with Europium Complexes. *Chem. Mater.* **2007**, *19*, 3892−3901.

(63) Binnemans, K.; Lenaerts, P.; Driesen, K.; Gorller-Walrand, C. A Luminescent Tris(2-thenoyltrifluoroacetonato) Europium(III) Complex Covalently Linked to a 1,10-phenanthroline-functionalised Sol-gel Glass. *J. Mater. Chem.* **2004**, *14*, 191−195.

(64) Supkowski, R. M.; Horrocks, W. D. On the Determination of the Number of Water Molecules, q, Coordinated to Europium(III) ions in Solution from Luminescence Decay Lifetimes. *Inorg. Chim. Acta* **2002**, *340*, 44−48.

(65) Reisfeld, R.; Shamrakov, D.; Jorgensen, C. Photostable Solar Concentrators based on Fluorescent Glass Films. *Sol. Energy Mater. Sol. C* **1994**, *33*, 417−427.